

Supporting Information for

Differential Enzyme Flexibility Probed using Solid-State Nanopores

Rui Hu^{1,2}, João V. Rodrigues³, Pradeep Waduge⁴, Hirohito Yamazaki⁴, Benjamin Cressiot⁴, Yasmin Chishti⁵, Lee Makowski⁵, Dapeng Yu^{1,2}, Eugene Shakhnovich³, Qing Zhao^{1,2*}, Meni Wanunu^{4*}

¹State Key Laboratory for Mesoscopic Physics and Electron Microscopy Laboratory, School of Physics, Peking University, Beijing 100871, People's Republic of China.

²Collaborative Innovation Center of Quantum Matter, 100084 Beijing, China.

³Department of Chemistry and Chemical Biology, Harvard University, Cambridge, MA 02138

⁴Department of Physics, Northeastern University, Boston, MA 02115, United States

⁵Department of Bioengineering, Northeastern University, Boston, MA 02115, United States

*Correspondence to: zhaoqing@pku.edu.cn; wanunu@neu.edu

Table of contents:

SI-1. The detail of finite element simulation based of velocity profile inside the nanopore using pressure flow and retarding electric field.

SI-2. Scatter plots, dwell histograms and first arrival distributions from pressure-assisted translocations for AdK-apo and AdK-Ap5A.

SI-3. The dependency of characteristic duration time of DHFR mutant L28R as a function of voltage.

SI-4. Voltage-independent FWHM values for wt DHFR originated from *Chlamydia muridarum* C7.

SI-5. Representative continuous current traces for DHFR mutants.

SI-6. The extent of proteolytic degradation of *E. coli* DHFR variants correlates with bis-ANS fluorescence intensity.

SI-7. Bis-ANS binding curves for different DHFR variants.

SI-1 Details of finite-element simulation of the velocity profile inside a nanopore using pressure-driven flow and a retarding voltage.

We used COMSOL Multiphysics to calculate the velocity profile inside the nanopore using the Navier-Stokes equation, the Nernst-Planck equation, and Poisson's equation. Specifically, we used the Transport of Diluted Species (chds), Laminar Flow (spf) and Electrostatics (chds) modules. Fig. S1 A and B show the geometry and the boundary condition for the simulation. A symmetrical model was used to reduce the simulation time. The entire nanopore length, h_{ent} , and the diameter of nanopore opening were defined as $3h_{eff}$ and $2d_p$, where h_{eff} and d_p are the effective nanopore thickness and diameter of nanopore. The entire nanopore length and diameter of nanopore are 21 and 7 nm. The surface charge of SiN was set to -11 mC/m^2 .¹ The upper boundary (*cis* chamber) was grounded with $V = 0$ and $P = 1 \text{ atm}$ (voltage-induced electrophoresis mode) or 3 atm (pressure-driven mode); the lower boundary (*trans* chamber) was set to $V = -50, -60, \text{ and } -70 \text{ mV}$ respectively with ambient pressure $P = 1 \text{ atm}$.

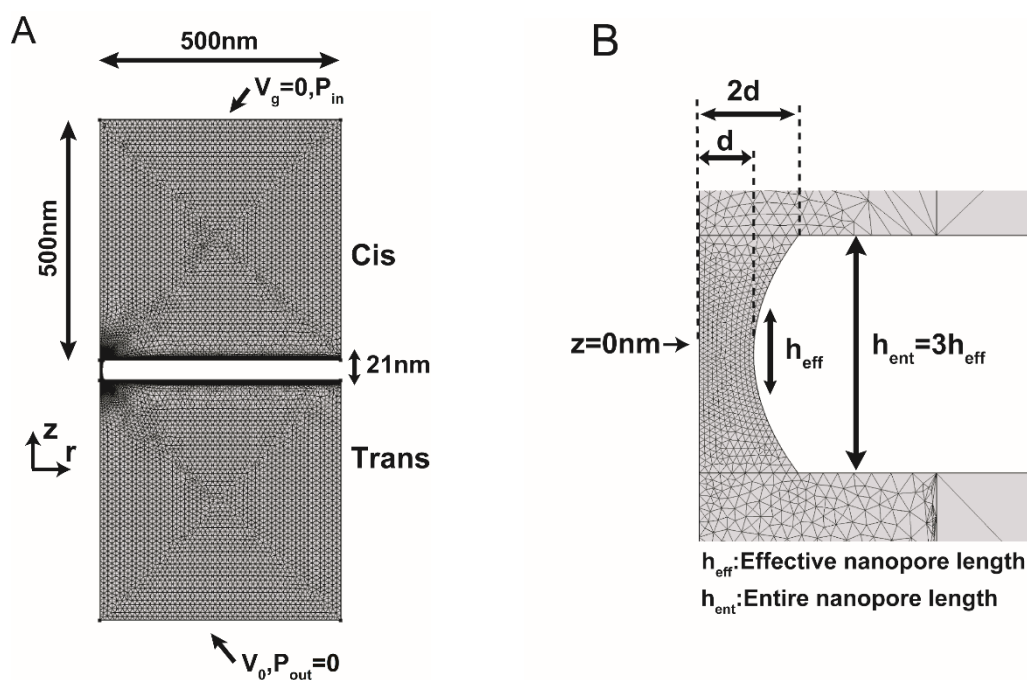


Figure S1. 2D model for osmosis velocity calculation. (A) Entire calculation model, and (B) nanopore geometry and all definitions of geometric variables.

SI-2 Scatter plots, dwell time histograms and first arrival time distributions of pressure-assisted translocations for AdK-*apo* and AdK-*Ap5A*.

Fig. S2A describes the scatter plots of translocation events for AdK-*apo* (yellow) and AdK-*Ap5A* (blue) with fractional blockade ($\Delta I/I_0$) as y axis and dwell time as x axis in log scale. It shows the majority of AdK-*Ap5A* translocations block less than AdK-*apo*, indicating the conformational change occurred upon Ap5A addition. The values of v and D in main test are extracted from dwell time histograms (Fig. S2B) based on one dimensional drift model,¹⁻² while R is obtained by fitting of first arrival time distributions (Fig. S2C) to single-exponential decay, as reported before.²⁻³

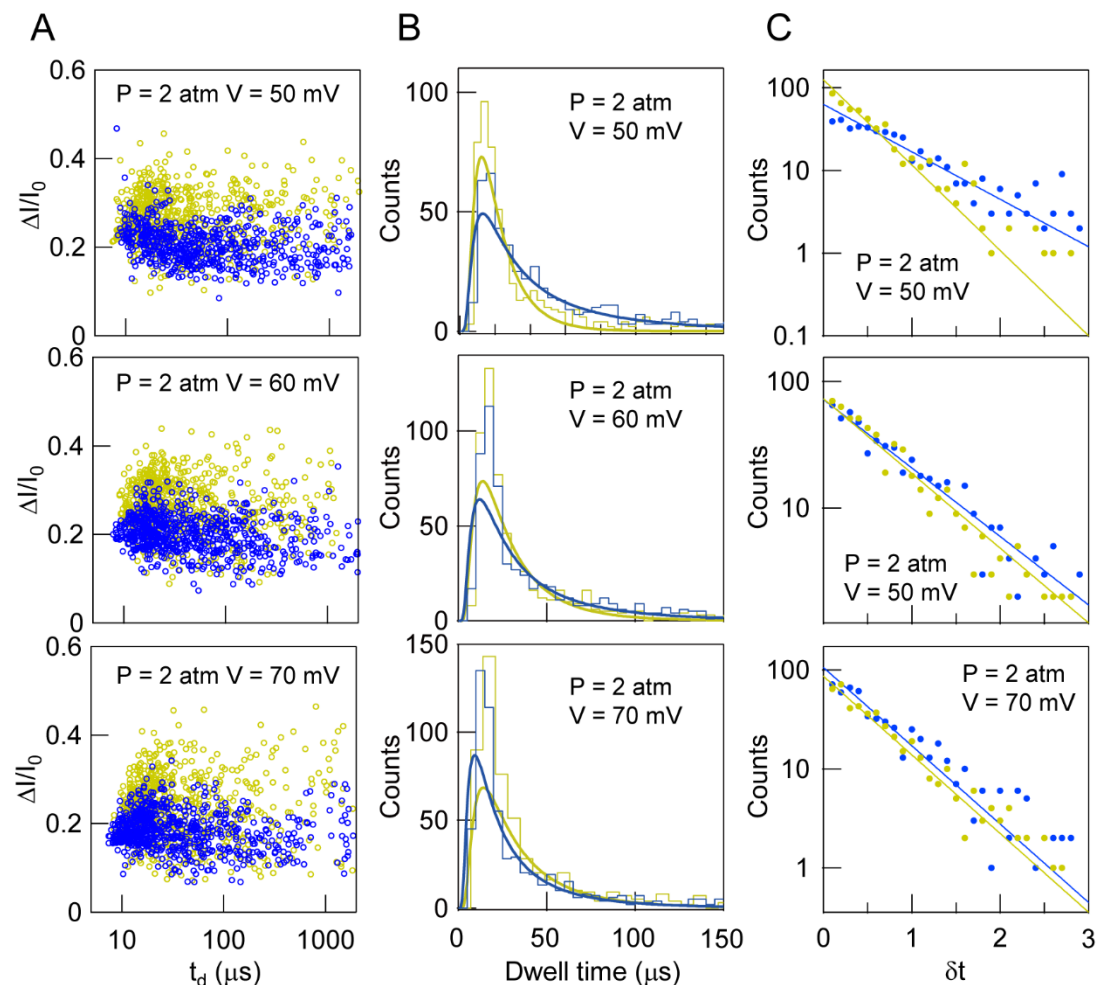


Figure S2. Pressure-driven translocations of AdK-*apo* and AdK-*Ap5A*. (A) Scatter plots of dwell-times (t_d) vs. fractional current blockades ($\Delta I/I_0$) for AdK-*apo* (yellow) and AdK-*Ap5A* (blue) translocations at $\Delta P = 2$ atm and retarding voltage values of 50 mV ($n_{\text{AdK-}apo}=623$, $n_{\text{AdK-}Ap5A}=615$), 60 mV ($n_{\text{AdK-}apo}=664$, $n_{\text{AdK-}Ap5A}=691$), and 70 mV ($n_{\text{AdK-}apo}=621$, $n_{\text{AdK-}Ap5A}=696$). (B) Dwell-time histograms and (C) Inter-event arrival time (δt) distributions of translocation events for AdK-*apo* (yellow) and AdK-*Ap5A* (blue) at $\Delta P = 2$ atm using different retarding voltages (as indicated). All data were low-pass filtered to 150 kHz.

SI-3 Voltage-independent FWHM values for wt DHFR originated from *Chlamydia muridarum* C7

Here we present voltage-dependence data for a more flexible DHFR at voltages of -200mV, -250 mV, and -300 mV. It shows that both FWHM values and $\langle \Delta I/I_0 \rangle$ values are voltage independent in this voltage range.

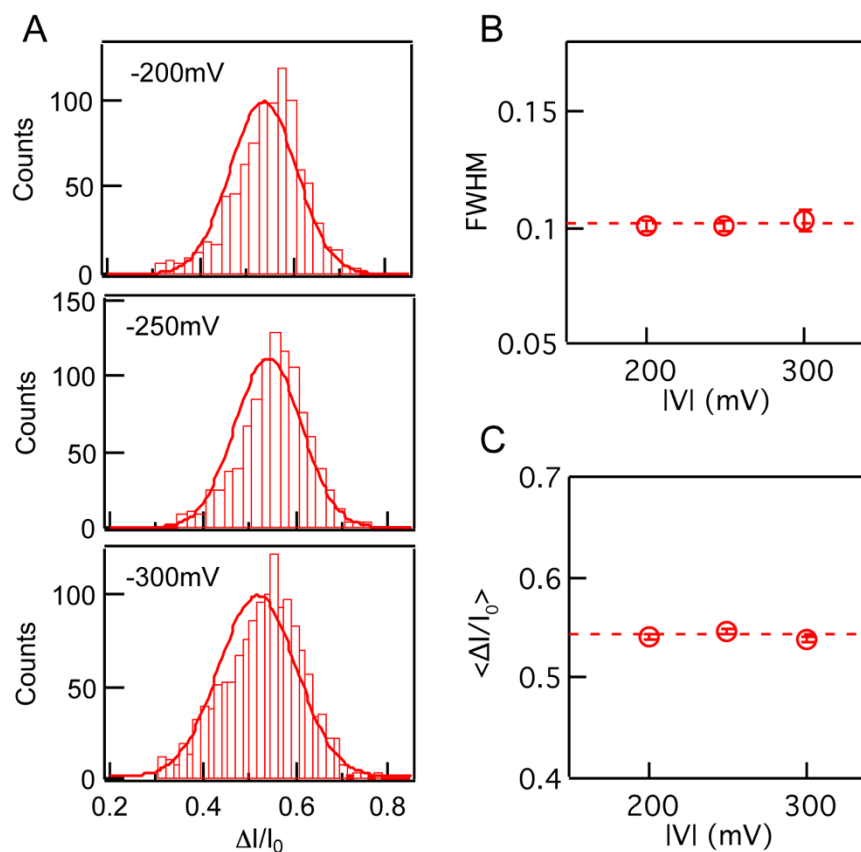


Figure S3. Voltage-independence of FWHM and $\langle \Delta I/I_0 \rangle$ values for wt DHFR originated from *Chlamydia muridarum* C7. (A) The plots of $\Delta I/I_0$ histograms at -200 mV, -250 mV and -300 mV. (B) Peak position and (C) FWHM extracted from Gaussian fitting of $\Delta I/I_0$ histogram as a function of absolute value of applied voltages.

SI-4 The dependency of characteristic duration time of DHFR mutant L28R as a function of voltage.

We fit the event duration histogram using $\sim \exp(-x/\tau)$ and plot the typical event duration τ as a function of voltage. (Fig. 2) We found that event duration is inversely proportional to the applied voltage, which can be described by electrophoretic transport.⁴

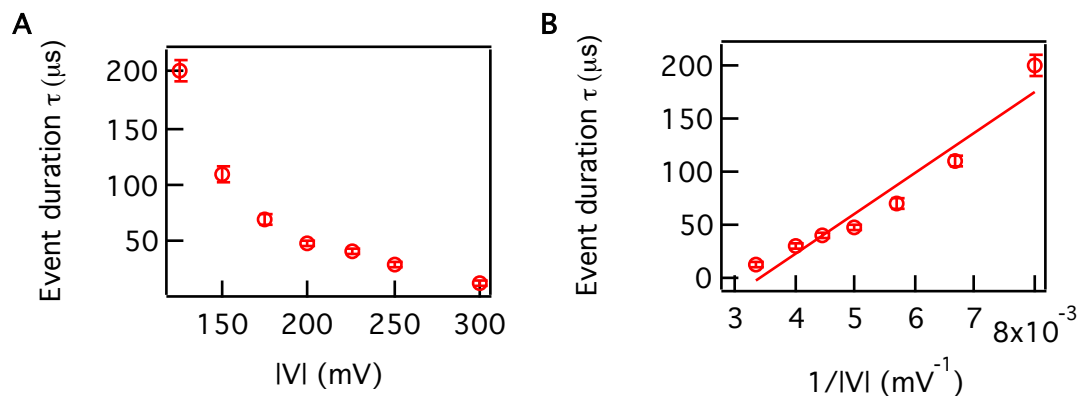


Figure S4. The dependency of characteristic duration time τ of DHFR mutant L28R as a function of voltage. Typical event duration τ as a function of the absolute value of A) applied voltage $|V|$ and B) inverse of $|V|$.

SI-5 Representative continuous current traces for DHFR mutants.

Here we present 8-second continuous current traces for DHFR E28T (E1) originated from *Escherichia coli*, DHFR wt (C7), and DHFR P21L (C9) originated from *Chlamydia muridarum* recorded at -200 mV and low-pass filtered to 250 kHz from pore 2 in main text. Current values were inverted for clarity.

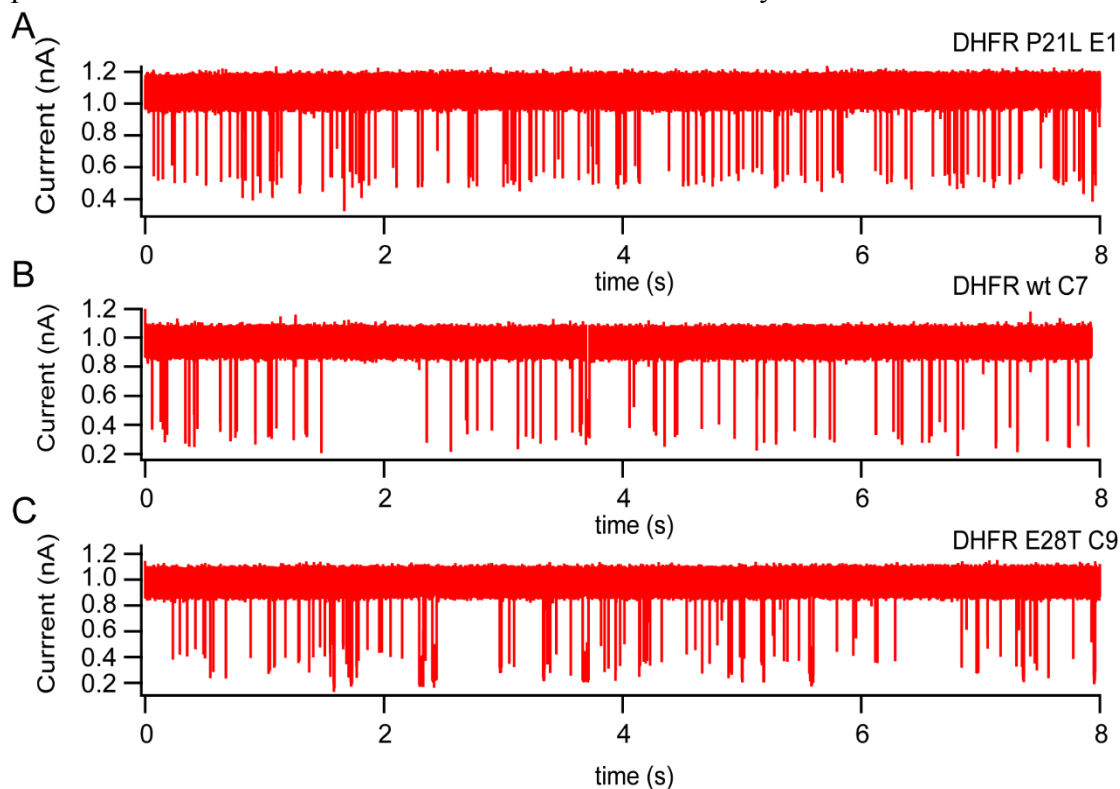


Figure S5. Representative continuous current traces for DHFR mutants.

Continuous current trace for (A) DHFR E28T, E1, originated from *Escherichia coli*, (B) wt DHFR C7 originated from *Chlamydia muridarum*, and (C) DHFR P21L, C9, originated from *Chlamydia muridarum*.

SI-6 The extent of proteolytic degradation of *E. coli* DHFR variants correlates with bis-ANS fluorescence intensity.

We carried out a limited proteolysis assay with a set of *E. coli* DHFR mutants to probe intermediates with high structural flexibility by bis-ANS fluorescence experiment, since these conformational states are known to be preferentially degraded by proteases. We observed a linear correlation between bis-ANS fluorescence and the extent of proteolytic digestion, which supports that bis-ANS intensity accurately reports DHFR molten globule intermediates that promote binding of a bis-ANS molecule.

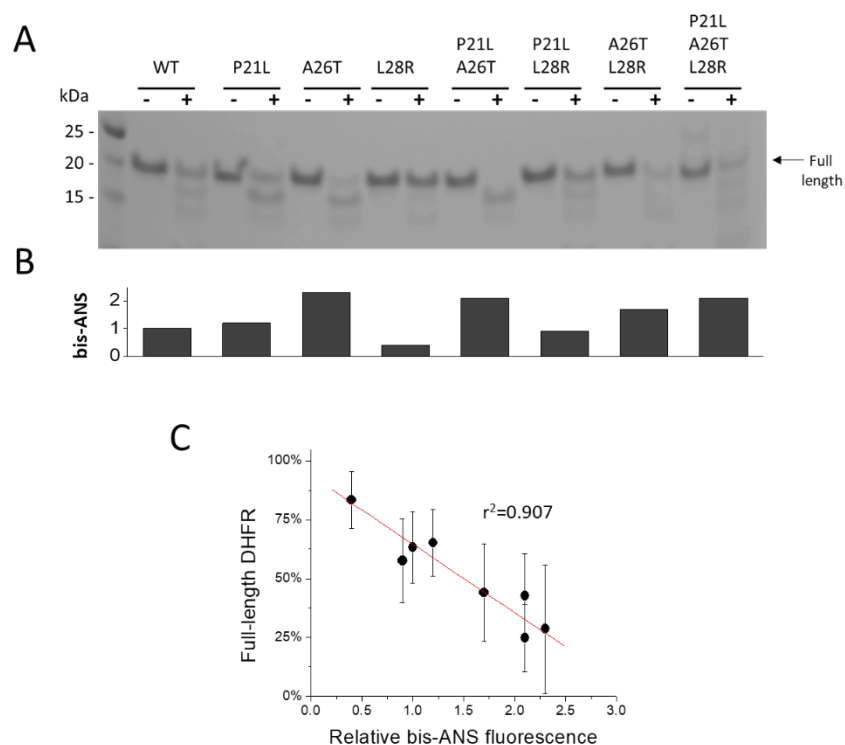


Figure S6 The extent of proteolytic degradation of *E. coli* DHFR variants correlates with bis-ANS fluorescence intensity. A) Limited proteolysis of DHFR variants analyzed by SDS-PAGE. Proteins (5 μ M) were digested with 1 μ M α -chymotrypsin at 20°C for 20 min. Reactions were quenched by the addition of SDS-containing loading buffer supplemented with protease inhibitors followed by boiling for 5 min under reducing conditions and analyzed by SDS-page. The extent of proteolysis was determined by quantification of the intensity of the band corresponding to the full-length protein in the treated (+) vs non-digested (-) samples. Values from 2 independent experiments were averaged. B) Relative bis-ANS fluorescence intensity measured for each DHFR variant. C) Extent of proteolytic degradation of DHFR as a function of bis-ANS fluorescence.

SI-7 Bis-ANS binding curves for different DHFR variants.

In order to address binding site numbers, we performed fluorescence-based bis-ANS titrations of three DHFR variants chosen to represent distinct bis-ANS fluorescence properties. Our results show that most bis-ANS fluorescence arises from binding of the dye to a single protein binding site. Moreover, for E coli WT and especially the L28R mutant, the number of available binding sites determined by fitting the data is lower than unity, suggesting that only a sub-population of the protein has high affinity for the dye. This is consistent with the existence of molten-globule intermediates in equilibrium with the native compact structure, again supporting our interpretation that bis-ANS fluorescence intensity data reflects the proportion of highly flexible intermediates in solution.

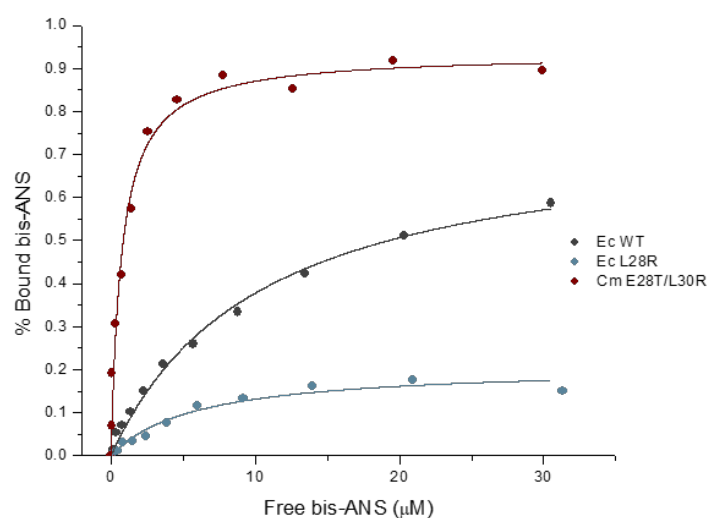


Figure S7 Bis-ANS binding curves for different DHFR variants. Protein solutions (2 μM) were incubated at 25°C in 100 mM Tris pH8.0 and titrated with increasing concentrations of bis-ANS and the resulting fluorescence spectra was recorded between 410 and 600 nm (excitation 395 nm). The area of the emission band was used to calculate the fraction of bound bis-ANS using a conversion factor determined by measuring the intensity of a 0.76 μM bis-ANS solution titrated to saturation with Cm E28T/L28R. One-binding site equations $y=nL/(k+L)$ were used to fit the data (Ec.WT $n= 0.77$, $k =10$ μM, Ec.L28R DHFR $n=0.26$, $k = 8.6$ μM, Cm.E28T/L28R $n = 0.93$, $k = 0.74$ μM).

References

1. Waduge, P.; Hu, R.; Bandarkar, P.; Yamazaki, H.; Cressiot, B.; Zhao, Q.; Whitford, P. C.; Wanunu, M., Nanopore-Based Measurements of Protein Size, Fluctuations, and Conformational Changes. *ACS Nano* **2017**, *11*, 5706-5716.
2. Larkin, J.; Henley, R. Y.; Muthukumar, M.; Rosenstein, J. K.; Wanunu, M., High-Bandwidth Protein Analysis Using Solid-State Nanopores. *Biophys. J.* **2014**, *106*, 696-704.
3. Meller, A.; Branton, D., Single Molecule Measurements of DNA Transport through a Nanopore. *Electrophoresis* **2002**, *23*, 2583-2591.
4. Cressiot, B.; Oukhaled, A.; Bacri, L.; Pelta, J., Focus on Protein Unfolding through Nanopores. *BioNanoScience* **2014**, 1-8.